



Cite this: *Chem. Commun.*, 2025, 61, 8671

Received 3rd March 2025,  
Accepted 9th May 2025

DOI: 10.1039/d5cc01147g

[rsc.li/chemcomm](http://rsc.li/chemcomm)

**Selective photoreduction of CO<sub>2</sub> to CO, CH<sub>4</sub>, and C<sub>2,3</sub> paraffins was directed by increasing ultraviolet-visible light intensity over an Fe–ZrO<sub>2</sub> photocatalyst. Fe<sup>0</sup> nanoparticles sequentially reduced COH—transferred from the ZrO<sub>2</sub> surface—into CH<sub>x</sub> species and hydrocarbons, facilitated by light-induced heating to ~452 K.**

Photocatalytic CO<sub>2</sub> reduction establishes a novel C-neutral cycle and is considered a potential environmental solution for a sustainable society.<sup>1,2</sup> However, its near-term implementation is hindered by economic challenges, primarily due to the costs of photocatalysts and reactor design.<sup>3,4</sup> Among first-row transition metals, Fe is the most abundant and cost-effective. Consequently, Fe-based photocatalysts for CO<sub>2</sub> photoreduction have been widely studied. However, nearly all reported systems employ Fe in the form of metal ions within metal–organic frameworks, covalent organic frameworks, porphyrins, or as Fe<sub>2</sub>O<sub>3</sub>, functioning primarily as redox mediators (Table S1, ESI†).<sup>5</sup>

In this study, a Fe<sup>0</sup> surface was evaluated as a CO<sub>2</sub> photoreduction catalyst for C<sub>1–3</sub> hydrocarbons (HCs) in combination with semiconductor ZrO<sub>2</sub>. An Fe<sub>3</sub>O<sub>4</sub>–ZrO<sub>2</sub> composite was synthesized *via* a liquid-phase reduction method, using Fe(NO<sub>3</sub>)<sub>3</sub>·9H<sub>2</sub>O as the precursor and reducing it at 973 K under H<sub>2</sub> to obtain the Fe<sup>0</sup> (7.5 wt%)-ZrO<sub>2</sub>-973R photocatalyst. The valence state and coordination of Fe were monitored during synthesis using X-ray absorption near-edge structure (XANES) and extended X-ray absorption fine structure (EXAFS).

This approach facilitated the formation of bifunctional sites—O vacancies (V<sub>O</sub><sup>•</sup>) on the ZrO<sub>2</sub> surface<sup>3,6–9</sup> and Fe<sup>0</sup> nanoparticles—enabling the selective photogeneration of CO and C<sub>1–3</sub> HCs from CO<sub>2</sub>. At a ultraviolet-visible (UV-Vis) light intensity of 110 mW cm<sup>−2</sup>, using <sup>13</sup>CO<sub>2</sub> and H<sub>2</sub> gases with the Fe<sup>0</sup> (7.5 wt %)-ZrO<sub>2</sub>-973R photocatalyst, both <sup>13</sup>CO and <sup>13</sup>CH<sub>4</sub>

## Light intensity–directed selective CO<sub>2</sub> photoreduction using iron(0)–zirconium dioxide photocatalyst†

Tomoki Oyumi, Ikki Abe, Masahito Sasaki and Yasuo Izumi \*

were gradually generated over the first 5 h of photoreaction (Table 1a). However, beyond this period, <sup>13</sup>CO formation became predominant (> 99 mol% selectivity; entry a'), as subsequent reaction steps from CO did not proceed (Scheme 1a). The steady photogeneration of CO was significantly faster than that observed with ZrO<sub>2</sub> alone (Table S2a, ESI†),<sup>6–8</sup> confirming the active role of the Fe<sup>0</sup> surface, but the selectivity change after 5 h seemed due to strong CO<sub>2</sub> adsorption on it in CO<sub>2</sub> photoreduction (see below).

In stark contrast, increasing the irradiated light intensity to 322 mW cm<sup>−2</sup> shifted the Fe<sup>0</sup>-ZrO<sub>2</sub>-973R photocatalyst from selective two-electron reduction to <sup>13</sup>CO to predominant eight-electron reduction to <sup>13</sup>CH<sub>4</sub> production (> 95 mol% selectivity; Table 1b). This shift occurred because the hydrogenation steps from CO proceeded rapidly under higher light intensity, facilitating the sequential reduction from CO<sub>2</sub> to CO and ultimately to CH<sub>4</sub>. From a practical perspective, however, the <sup>13</sup>CH<sub>4</sub> light-induced synthesis using Fe<sup>0</sup>-ZrO<sub>2</sub> requires further improvement, as photocatalytic activity declined after 5 h of photoreaction—more so than under 110 mW cm<sup>−2</sup> irradiation (Table 1a' and b'). As no CH<sub>x</sub> species were observed in the Fourier transform infrared (FTIR) spectrum under the conditions, this deactivation was attributed to Fe<sup>0</sup> surface poisoning by strongly adsorbed CO<sub>2</sub> (Scheme 1b).

To enhance the stability of the Fe<sup>0</sup>-ZrO<sub>2</sub>-973R photocatalyst, the irradiated light intensity was further increased to 472 mW cm<sup>−2</sup>. Under these conditions, the <sup>13</sup>CH<sub>4</sub> formation rate reached 170  $\mu\text{mol h}^{-1} \text{g}_{\text{cat}}^{-1}$  with > 71 mol% selectivity, accompanied by <sup>13</sup>CO formation at 69  $\mu\text{mol h}^{-1} \text{g}_{\text{cat}}^{-1}$  (> 28 mol% selectivity) over 5 h of photoreaction (Fig. 1A and Table 1c). Over time, <sup>13</sup>CH<sub>4</sub> formation exhibited a turning point at ~ 5 h of photoreaction (Fig. 1A), attributed to partial Fe<sup>0</sup> site poisoning by intermediate species such as HCO<sub>2</sub> and CH<sub>x</sub>. Beyond this period, the <sup>13</sup>CH<sub>4</sub> formation rate stabilized at 20  $\mu\text{mol h}^{-1} \text{g}_{\text{cat}}^{-1}$  with > 49 mol% selectivity (Table 1c' and Scheme 1c). Under the steady conditions, CO<sub>2</sub> blocking on Fe<sup>0</sup> sites should be less effective in contrast to the status under 110–322 mW cm<sup>−2</sup> irradiation. This time-dependent product distribution confirmed a consecutive

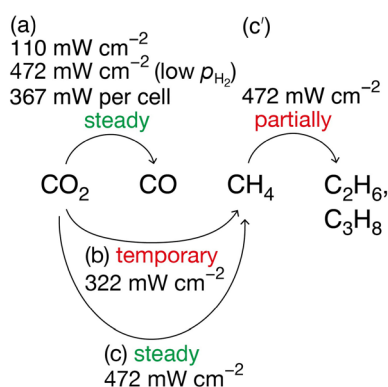
Department of Chemistry, Graduate School of Science, Chiba University, Yayoi 1-33, Inage-ku, Chiba 263-8522, Japan. E-mail: [yizumi@faculty.chiba-u.jp](mailto:yizumi@faculty.chiba-u.jp)

† Electronic supplementary information (ESI) available: Lists of reported photo- and thermal catalysts, experimental details, photocatalytic time course, X-ray diffraction, and optical, X-ray absorption, and FTIR spectroscopy of photocatalyst and surface species. See DOI: <https://doi.org/10.1039/d5cc01147g>



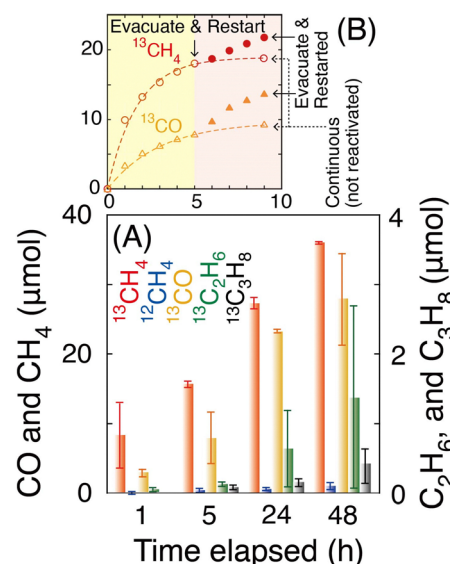
Table 1  $\text{CO}_2$  photoreduction outcomes using  $\text{Fe}$  (7.5 wt%)– $\text{ZrO}_2$  prerduced at 973 K in the presence of either  $\text{H}_2$  or  $\text{H}_2\text{O}$ 

Entry	Reactant	Reducant	Light intensity (mW)	Stage of reaction test (h)	Formation rate ( $\mu\text{mol h}^{-1} \text{g}_{\text{cat}}^{-1}$ )				
					$^{13}\text{CO}$	$^{13}\text{CH}_4$	$^{13}\text{C}_2\text{H}_6$	$^{13}\text{C}_3\text{H}_8$	$\text{O}_2$
a	$^{13}\text{CO}_2$ (2.3 kPa)	$\text{H}_2$ (21.7 kPa)	110 $\text{cm}^{-2}$	0–5	3.7	3.8	0.052	0.018	<0.002
a'			322 $\text{cm}^{-2}$	5–48	3.7	<0.002	<0.002	<0.002	
b			322 $\text{cm}^{-2}$	0–5	2.4	45	0.20		
b'			472 $\text{cm}^{-2}$	5–48	1.7	1.1	0.036		
c			472 $\text{cm}^{-2}$	0–5	69	170	2.1	0.30	
c'			472 $\text{cm}^{-2}$	5–48	18	20	2.3	0.56	
c''			472 $\text{cm}^{-2}$	(20–48)	(2.7)	(16)	(2.6)	(0.70)	
d			1510 $\text{cm}^{-2}$	0–5	35	40	0.26	<0.002	<0.002
d'			1510 $\text{cm}^{-2}$ (with water bath)	5–48	5.2	0.41	0.037		
e	$\text{CO}_2$ (95 kPa)	$\text{H}_2\text{O}$ (70 mL)	367 per cell	0–5	CO	$\text{CH}_4$	$\text{C}_2\text{H}_6$	$\text{C}_3\text{H}_8$	$\text{O}_2$
e'			367 per cell	5–48	12	<0.002	<0.002		64
					8.5	0.86			9.0

Scheme 1 Temporary and steady  $\text{CO}_2$  photoreduction pathways directed by irradiated light intensity (110–472  $\text{mW cm}^{-2}$ ) using the  $\text{Fe}^0$  (7.5 wt%)– $\text{ZrO}_2$ -973R photocatalyst in presence of  $\text{H}_2$  (a)–(c) and (c') or  $\text{H}_2\text{O}$  (a).

reaction pathway:  $\text{CO}_2$  reduction to  $\text{CO}$ , followed by  $\text{CH}_4$  formation, and subsequent conversion to  $\text{C}_{2,3}$  hydrocarbons. Between 20 and 48 h of photoreaction, the  $^{13}\text{CH}_4$  formation rate remained stable (> 73 mol% selectivity), while  $^{13}\text{C}_2\text{H}_6$  and  $^{13}\text{C}_3\text{H}_8$  selectivity significantly increased to 15 mol% (total formation rate: 3.3  $\mu\text{mol h}^{-1} \text{g}_{\text{cat}}^{-1}$ ), effectively suppressing initial  $^{13}\text{CO}$  production (Table 1c'' and Scheme 1c'). Notably, no  $\text{C}_2\text{H}_4$  or  $\text{C}_3\text{H}_6$  was detected. Furthermore, photocatalytic activity could be restored by a 1-h evacuation at  $10^{-6}$  Pa under light, reactivating the consecutive reduction process from  $\text{CO}$  to  $\text{CH}_4$  (Fig. 1B).

The other photocatalytic test was using  $\text{CO}_2$  (2.3 kPa),  $\text{H}_2$  (21.7 kPa), and the light irradiation at 1510  $\text{mW cm}^{-2}$ , but the quartz reactor was cooled with water bath (Table 1d–d' and Chart S1, ESI†). The  $^{13}\text{CO}$  and  $^{13}\text{CH}_4$  formation rates were 24–51% of corresponding rates without water cooling until 5 h of reaction (Table 1c and c'), while the decline after 5 h was more significant, especially for  $^{13}\text{CH}_4$  formation, strongly suggesting that charge separation in/on  $\text{ZrO}_2$  owing to light proceeded  $\text{CO}_2$  reduction while  $\text{Fe}$  nanoparticle surface at lower temperature in thermal equilibrium with  $\text{ZrO}_2$ , reactor, and 2.5 L of water was deactivated for subsequent multiple hydrogenation earlier by adsorbed species, *e.g.*  $\text{CO}_2$ . The increase of water temperature was minimal: from 295.2 to 295.5 K during the photocatalytic test for 48 h (Chart S1, ESI†).

Fig. 1 (A) and (B) Time course of  $^{13}\text{CO}$ ,  $^{13}\text{CH}_4$ ,  $^{12}\text{CH}_4$ ,  $^{13}\text{C}_2\text{H}_6$ , and  $^{13}\text{C}_3\text{H}_8$  formation using  $\text{Fe}^0$  (7.5 wt%)– $\text{ZrO}_2$ -973R,  $^{13}\text{CO}_2$  (2.3 kPa),  $\text{H}_2$  (21.7 kPa), and UV-Vis light irradiation at 472  $\text{mW cm}^{-2}$ . (B) Comparison with the reactivation test (filled symbols) after 1 h of catalyst evacuation under UV-Vis light irradiation at the 5-h mark.

Steady photocatalytic  $\text{CO}_2$  reduction was also achieved using  $\text{H}_2\text{O}$  as the reductant instead of  $\text{H}_2$  under UV-Vis light irradiation at 367  $\text{mW per cell}$ .  $\text{CO}$  was continuously generated at a rate of 12–8.5  $\mu\text{mol h}^{-1} \text{g}_{\text{cat}}^{-1}$  (Table 1e and e'), proceeding more rapidly than the multiple hydrogenation steps required for  $\text{CH}_4$  formation over  $\text{Fe}^0$  (selectivity < 9.2 mol%; Scheme 1a and Fig. S1, ESI†). This was attributed to the predominant presence of  $\text{H}_2\text{O}$  rather than  $\text{H}$  at the  $\text{Fe}^0$  surface, which favored  $\text{CO}$  generation over further hydrogenation to  $\text{CH}_4$ .

The effects of UV-Vis light irradiation on the  $\text{Fe}^0$ – $\text{ZrO}_2$ -973R photocatalyst were investigated. In the UV-Vis absorption spectra of the  $\text{Fe}_3\text{O}_4$ – $\text{ZrO}_2$  sample (Fig. S2b, ESI†), two absorption shoulders at 410 and 525 nm, attributed to  $\text{Fe}^{2+}$  and  $\text{Fe}^{3+}$  ions, were observed, whereas  $\text{ZrO}_2$  alone exhibited no visible light absorption (spectrum a). This spectral profile was consistent with the reported absorption spectrum of  $\text{Fe}_3\text{O}_4$ .<sup>10</sup> Upon  $\text{H}_2$  treatment at 973 K, absorption extended across the entire visible region



(spectrum c), and the spectrum remained similar after 48 h of photocatalytic  $^{13}\text{CO}_2$  reduction (spectrum d), confirming the formation and stability of  $\text{Fe}^0$  nanoparticles, which facilitated multiple hydrogenation steps from CO/COH species (Scheme 1c and c'). The Fe valence state assignments were corroborated by changes in the XANES spectrum, aligning with those of standard  $\text{Fe}^0$  and  $\text{Fe}_3\text{O}_4$  (Fig. S3A(c) and (d), ESI $^\dagger$ ).<sup>11</sup> EXAFS Fourier transform analysis of  $\text{Fe}^0\text{-ZrO}_2\text{-973R}$  revealed interatomic pairs characteristic of  $\text{Fe}^0$  (Fig. S4, ESI $^\dagger$ ), while X-ray diffraction showed an Fe (011) peak overlapping with peaks corresponding to monoclinic  $\text{ZrO}_2$  (Fig. S5, ESI $^\dagger$ ), further supporting the formation of  $\text{Fe}^0$  active sites in the  $\text{Fe}^0\text{-ZrO}_2\text{-973R}$  photocatalyst.

The fluorescence emission spectra of  $\text{Fe}^0\text{-ZrO}_2\text{-973R}$  were measured under excitation at 200 nm (Fig. S6, ESI $^\dagger$ ), a wavelength corresponding to an energy higher than the band gap of  $\text{ZrO}_2$  (Fig. S2a, ESI $^\dagger$ ). The spectrum exhibited both an interband excitation-deexcitation peak centered at 367 nm (spectrum a) and intraband transition peaks associated with impurity levels, such as O vacancies and Hf (0.55 wt%) in/on  $\text{ZrO}_2$ , appearing at 451, 468, 481, 491, 528, and 623 nm. These emissions were significantly suppressed upon the addition of  $\text{Fe}_3\text{O}_4$  and further reduced with  $\text{Fe}^0$  nanoparticles (spectra b and c), indicating effective trapping of excited electrons at the conduction band (CB) of  $\text{ZrO}_2$ .

Next, the reaction pathway from  $\text{CO}_2$  to CO and HCs is considered. The role of  $\text{V}_\text{O}^\bullet$  sites on the  $\text{ZrO}_2$  surface in  $\text{CO}_2$  adsorption and its subsequent photoreduction to OCOH and COH species was analyzed using density functional theory (DFT) calculations.<sup>9</sup> The population of surface  $\text{V}_\text{O}^\bullet$  sites was evaluated to one per 44 nm $^2$  based on  $^{13}\text{CO}_2$  exchange amount with preadsorbed  $^{12}\text{CO}_2$  on  $\text{V}_\text{O}^\bullet$  site (0.070  $\mu\text{mol}$ ; Table S3g and Fig. S7, ESI $^\dagger$ ). The population of surface  $\text{V}_\text{O}^\bullet$  sites seems not vary much before and after photocatalytic test based on essentially negligibly-changing UV-visible and XRD data (Fig. S2c, d and S5a, b, ESI $^\dagger$ ). Consequently, this study focuses on the critical steps enabling transient or sustained  $\text{C}_{1-3}$  photogeneration (Scheme 1b and c), specifically the conversion of COH and/or CO into  $\text{C}_{1-3}$  HCs over the  $\text{Fe}^0$  surface.

To identify the active sites responsible for these reaction steps, Fe K-edge EXAFS measurements were conducted on the  $\text{Fe}^0\text{-ZrO}_2\text{-973R}$  photocatalyst under  $\text{CO}_2$  and  $\text{H}_2$  exposure. Unexpectedly,  $\sim 20\%$  of the  $\text{Fe}^0$  sites reduced at 973 K were oxidized upon reaction with  $\text{CO}_2$  in the dark, as indicated by EXAFS analysis (Fig. 2A, 0 min). The spectral fit, obtained by convolving standard XANES spectra for  $\text{Fe}^0$  and  $\text{FeO}$  with an 8:2 mixing ratio (Fig. S3B(d), ESI $^\dagger$ ), aligned with the EXAFS data. This oxidation is attributed to the formation of an M-shaped  $\text{Fe}^{2+}\text{-O-C}(\text{---Fe}^0)\text{-O-Fe}^{2+}$  species upon  $\text{CO}_2$  adsorption on Fe. DFT calculations further support the energetic stability of this species on the  $\text{Fe}^0$  (111) surface, with an adsorption energy of 0.92 eV and a Bader charge of +0.352 on Fe bonded to O, consistent with prior studies.<sup>12</sup> At this stage, CO did not desorb spontaneously from Fe surface and was not detected.

Upon UV-Vis light irradiation, the Fourier transform of EXAFS spectra (Fig. 2A, 0 min) showed that the Fe-O and  $\text{Fe}\cdots\text{Fe}$  peaks corresponding to  $\text{FeO}$  were rapidly replaced by

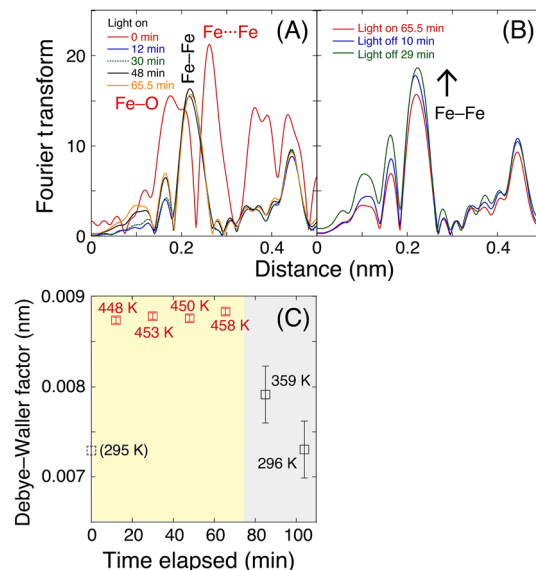


Fig. 2 Time-dependent Fourier transform of Fe K-edge EXAFS for  $\text{Fe}^0$  (7.5 wt%)- $\text{ZrO}_2\text{-973R}$  under  $\text{CO}_2$  (2.3 kPa),  $\text{H}_2$  (21.7 kPa), and UV-Vis light irradiation ( $322 \text{ mW cm}^{-2}$ ). (A) During 75 min of illumination, (B) after the light was turned off, and (C) corresponding time-dependent evolution of the Debye–Waller factor for the Fe–Fe interatomic pair.

a metallic Fe–Fe peak at 0.21 nm (phase shift uncorrected; Fig. 2A, 12 min). This transformation indicates the reduction of  $\text{Fe}^{2+}$  in the M-shaped  $\text{Fe}^{2+}\text{-O-C}(\text{---Fe}^0)\text{-O-Fe}^{2+}$  species.

In the FTIR spectrum of  $\text{Fe}^0\text{-ZrO}_2\text{-973R}$  under  $^{13}\text{CO}_2$  and  $\text{H}_2$  (Fig. S8, ESI $^\dagger$ ), shoulder peaks at 1584, 1396, and 1217  $\text{cm}^{-1}$  corresponded to  $\nu_\text{as}(\text{OCO})$ ,  $\nu_\text{s}(\text{OCO})$ , and  $\delta(\text{OH})$  bending vibrations, respectively, were attributed to monodentate and bridging bicarbonate species adsorbed on the surface.<sup>6-8</sup> In contrast, the broader peaks centered at 1538 and 1261  $\text{cm}^{-1}$  were tentatively assigned  $\nu_\text{as}(\text{OCO})$  and  $\nu_\text{s}(\text{OCO})$  stretching vibrations of bidentate carbonate species on  $\text{ZrO}_2$ ,<sup>13</sup> as well as the M-shaped  $\text{Fe-O-C}(\text{---Fe}^0)\text{-O-Fe}$  species proposed earlier, adsorbed at various sites on the  $\text{Fe}^0$  surface. This assignment aligns with DFT-calculated O–C–O bond angles of  $122^\circ$ . Upon UV-Vis light irradiation ( $265 \text{ mW cm}^{-2}$ ), the peak associated with  $^{13}\text{CO}_2$  and  $\text{H}_2$  adsorption negatively shifted by  $41 \text{ cm}^{-1}$ . This shift was attributed to the reduction of  $\text{Fe}^{2+}$  to  $\text{Fe}^0$  via electron transfer from  $\text{ZrO}_2$  CB to Fe, followed by electron injection into the  $\sigma^*$  orbitals of C–O bonds, facilitating bond weakening and activation under UV-Vis illumination, in consistent with the reduction from  $\text{Fe}^{2+}$  to  $\text{Fe}^0$  upon the light irradiation based on EXAFS (Fig. 2A).

The broad peak centered at  $1497 \text{ cm}^{-1}$  disappeared within 4 min under vacuum and UV-Vis light irradiation, likely due to  $\text{CO}_2$  desorption, suggesting that  $\text{CO}_2$  and carbonate species are not direct intermediates in  $\text{C}_{1-3}$  HC formation. In contrast, the conversion of adsorbed  $\text{CO}_2$  on the  $\text{ZrO}_2$  surface to COH species appears to be the rate-limiting step, as only methane ( $\nu_3$  peak at  $3010 \text{ cm}^{-1}$ ) was detected alongside adsorbed  $\text{CO}_2$  and bicarbonate species.

To elucidate the energetic origins of the multiple hydrogenation steps in which COH and/or CO species migrate over the  $\text{Fe}^0$  surface to form HCs, the Fe–Fe coordination number was



determined *via* EXAFS as 5.3, corresponding to a surface dispersion of 0.95.<sup>14</sup> In the correlated Debye model, the Debye temperatures of bulk and surface Fe (vertical motion) are reported as 467 K<sup>15</sup> and 225 K,<sup>16</sup> respectively. Using multiple scattering calculation code FEFF<sup>17</sup> and plane-wave EXAFS analysis code XDAP,<sup>18</sup> the local Fe site temperature during CO<sub>2</sub> photoreduction was experimentally monitored. Upon UV-Vis light irradiation, the Fe site temperature rapidly increased to  $\sim$  452 ( $\pm$ 35) K as hot spot due to light absorption and remained nearly constant at thermal equilibrium with the supporting ZrO<sub>2</sub> and the EXAFS cell both at  $\sim$  295 K (Fig. 2C, left).

When the light was turned off, the heat generated by light energy dissipated, and the Fe site temperature returned to 296 K (Fig. 2C, right). This observation confirms that the selective formation of C<sub>1–3</sub> HC<sub>s</sub> in this study resulted from a two-step process: (i) CO<sub>2</sub> reduction to COH/CO *via* charge separation in ZrO<sub>2</sub><sup>3,6–8</sup> and (ii) subsequent multiple hydrogenation of CO/COH on the Fe<sup>0</sup> surface, which was maintained at  $\sim$  452 K due to light absorption.

Thermal CO<sub>2</sub> hydrogenation and Fischer–Tropsch synthesis of HC(s) using Fe-based catalysts typically require reaction temperatures above 548 K (Table S4, ESI<sup>†</sup>) to achieve HC formation rates comparable to the Fe site temperature ( $\sim$  452 K, Fig. 2C) and the observed rate of 0.24 mmol h<sup>−1</sup> g<sub>cat</sub><sup>−1</sup> (Table 1c) in this study. Under CO<sub>2</sub> photoreduction conditions, Fe sites remained exclusively in the Fe<sup>0</sup> state (Fig. 2A and B), whereas thermal CO<sub>2</sub> reduction commonly involves Fe oxides and carbides (Table S4, ESI<sup>†</sup>). While the initial reduction of the first O atom in CO<sub>2</sub> over Fe<sup>0</sup> surfaces<sup>19</sup> typically requires high temperatures ( $>548$  K),<sup>20</sup> this study demonstrates that the first reduction step was instead facilitated by charge separation at V<sub>O</sub><sup>•</sup> sites on the ZrO<sub>2</sub> surface under light irradiation, enabling the reaction:



as previously reported.<sup>9</sup> This step was particularly effective at lower light intensities (110–322 mW cm<sup>−2</sup>; Table 1a–b') in the presence of neighboring Fe<sup>0</sup> nanoparticles. The subsequent hydrogenation pathway, where COH migrates to Fe<sup>0</sup> and undergoes further reduction to C<sub>1–3</sub> HC<sub>s</sub>, is likely a common feature in both thermal (Table S4, ESI<sup>†</sup>) and photo ( $\sim$  452 K, Fig. 2C) reactions, regardless of whether H<sub>2</sub> or H<sub>2</sub>O serves as the reductant.

The authors are grateful for the financial support from the Grant-in-Aid for Scientific Research B (24K01522, 20H02834, YI) from the Japan Society for the Promotion of Science. X-ray absorption experiments were performed with the approval of

the Photon Factory Proposal Review Committee (2024G067, 2022G527, 2021G546). The authors would like to thank Enago ([www.enago.jp](http://www.enago.jp)) for the language review.

## Data availability

The supporting data have been included as part of the ESI.<sup>†</sup>

## Conflicts of interest

There are no conflicts to declare.

## References

- Y. Izumi, *Coord. Chem. Rev.*, 2013, **257**, 171–186.
- Y. Izumi, in *Advances in CO<sub>2</sub> Capture, Sequestration, and Conversion*, ed. F. Jin, L.-N. He and Y. H. Hu, ACS Symposium Series, ACS Publications, 2015, ch. 1, vol. 1194, pp. 1–46.
- T. Loumisse, R. Ishii, K. Hara, T. Oyumi, I. Abe, C. Li, H. Zhang, R. Hirayama, K. Niki, T. Itoi and Y. Izumi, *Angew. Chem., Int. Ed.*, 2024, **63**, e202412090.
- J. Albero, Y. Peng and H. García, *ACS Catal.*, 2020, **10**, 5734–5749.
- L. H. M. de Groot, A. Ilic, J. Schwarz and K. Wärnmark, *J. Am. Chem. Soc.*, 2023, **145**, 9369–9388.
- H. Zhang, T. Itoi, T. Konishi and Y. Izumi, *Angew. Chem., Int. Ed.*, 2021, **60**, 9045–9054.
- H. Zhang, T. Itoi, K. Niki, T. Konishi and Y. Izumi, *Catal. Today*, 2020, **356**, 544–556.
- H. Zhang, T. Itoi, T. Konishi and Y. Izumi, *J. Am. Chem. Soc.*, 2019, **141**, 6292–6301.
- K. Hara, M. Nozaki, T. Hirayama, R. Ishii, K. Niki and Y. Izumi, *J. Phys. Chem. C*, 2023, **127**, 1776–1788.
- A. Bouafia, S. E. Laouini, A. Khelef, M. L. Tedjani and F. Guemari, *J. Cluster Sci.*, 2021, **32**, 1033–1041.
- Provided by Dr. Y. Niwa, High Energy Accelerator Research Organization.
- C. R. Kwawu, R. Tia, E. Adei, N. Y. Dzade, C. R. A. Catlow and N. H. de Leeuw, *Phys. Chem. Chem. Phys.*, 2017, **19**, 19478–19486.
- S. E. Collins, M. A. Baltanas and A. L. Bonivardi, *J. Catal.*, 2004, **226**, 410–421.
- B. J. Kip, F. B. M. Duivenvoorden, D. C. Koningsberger and R. Prins, *J. Catal.*, 1987, **105**, 26–38.
- American Institute of Physics Handbook*, ed. D. E. Gray, B. H. Billings, H. P. R. Frederikse, D. F. Bleil, R. B. Lindsay, R. K. Cook, J. B. Marion, H. M. Crosswhite and M. W. Zemansky, McGraw-Hill, New York, USA, 1972, 3rd edn, pp. 4–115.
- D. P. Jackson, *Surf. Sci.*, 1974, **43**, 431–440.
- L. Ankudinov, B. Ravel, J. J. Rehr and S. D. Conradson, *Phys. Rev. B: Condens. Matter Mater. Phys.*, 1998, **58**, 7565–7576.
- M. Vaarkamp, H. Linders and D. Koningsberger, *XDAP Version 3.2.9*, XAFS Services International, Woudenberg, The Netherlands, 2022.
- L. Krauser, Q. W. Yang and E. V. Kondratenko, *ChemCatChem*, 2024, **16**, e202301716.
- C. R. Kwawu, A. Aniagyei, R. Tia and E. Adei, *Mater. Renew. Sustainable Energy*, 2020, **9**, 4.